13th International Symposium on Turbulence and Shear Flow Phenomena (TSFP13)
Montreal, Canada, June 25–28, 2024

ACTIVE GENERATION OF DYNAMIC YAW, GUSTS, AND TURBULENCE IN A THREE-QUARTER OPEN-JET WIND TUNNEL

Germiel Cacho
Department of Mechanical Engineering
York University
4700 Keele St., Toronto, Ontario
gcacho@yorku.ca

Joshua Marques
Department of Mechanical Engineering
York University
4700 Keele St., Toronto, Ontario
jm96@yorku.ca

David Van Every
Process Engineering Group
Aiolos Engineering Corporation
135 Queen's Plate Dr., Unit 300, Toronto
david@aiolos.com

Peter Waudby-Smith
Process Engineering Group
Aiolos Engineering Corporation
135 Queen's Plate Dr., Unit 300, Toronto
Peter.Waudby-Smith@aiolos.com

Ronald E. Hanson
Department of Mechanical Engineering
York University
4700 Keele St., Toronto, Ontario
hansonre@yorku.ca

ABSTRACT

The following paper explores the flow characteristics in the test section of a three-quarter, open-jet, closed-loop return model wind tunnel at York University. The tunnel has a novel apparatus comprising three subsystems to generate transient yaw, gusts, and turbulence. The effect of each of the three subsystems on the resulting turbulent and unsteady flows is evaluated individually. It is shown that the Turbulence Generation System can generate yaw distributions with standard deviations ranging from 2.1 to 4 degrees, from the baseline passive case to those with oscillating airfoils. Frequency sweeping by the active yaw subsystem can fill a wide range of low-frequency spectra, otherwise populated with distinct frequencies and harmonics for discrete frequency forcing cases. The active gust subsystem causes unsteady gusts of over 15 percent of the mean flow velocity. In addition, the active turbulence subsystem generates turbulence intensities from a few percent passively to over 20 percent when operated actively. Intensity levels and length scales can be tailored depending on input parameters to the active grid.

INTRODUCTION

Vehicles operating on roadways are invariably subject to various dynamic airflow phenomena that can impact their aerodynamic performance. The airflow characteristics experienced by a moving vehicle depend on various influencing factors, including wind speed, wind direction, meteorological conditions, traffic density, road surface topography, and neighbouring vehicles. For a comprehensive review of this topic, readers are referred to the studies conducted by Cooper & Watkins (2007), Wordley & Saunders (2009) and Sims-Williams (2011), among others. The variable airflow conditions on-road vehicles encounter significantly impact aerodynamic performance, such as the vehicle's drag coefficient (Duncan *et al.*, 2017).

The on-road airflow conditions experienced by vehicles include variations in turbulence, with values from a few percent to values of 15% (Wordley & Saunders, 2009) or greater when close to other vehicles (Jessing *et al.*, 2020). Yaw variations generally are within ten degrees and follow a normal distribution (Cooper & Watkins, 2007; Wordley & Saunders, 2009) on highways. However, for various driving conditions, such as following another vehicle or overtaking, broader yaw distributions are found (Jessing *et al.*, 2020). Streamwise length scales extend from fine to multiple vehicle lengths, as shown by Wordley & Saunders (2009). The resulting on-road spectra reflect the presence of these scales and turbulence intensity. Sims-Williams (2011) demonstrated the importance of the low-frequency range of the on-road spectra regarding potential unsteady aerodynamic response.

Vehicle aerodynamic testing often employs wind tunnels that provide uniform and low turbulence conditions that emulate the flow experienced by isolated on-road vehicles while travelling at a constant speed and direction without wind. However, some wind tunnels intended for land vehicle testing contain systems to produce transient flow behaviour and turbulence. For example, wind tunnel passive turbulence generation systems use static drag-based or bluff body flow elements like spires, bars, or nets placed at the nozzle (McAuliffe *et al.*, 2014, for example). Another example is a system with components resembling activated spires that can morph in width, which was shown to generate a wide range of turbulent flow parameters (Cogetti, 2003). An advantage of active

input for automotive wind tunnels is the input of energetic low-frequency turbulent scales that capture elements of observed on-road flow fields. Given the emphasis on replicating transient yaw observed on-road, wind tunnel systems with activated airfoils have been designed to yaw the flow dynamically (Blumrich *et al.*, 2015; Terakado *et al.*, 2017, for example). The system of Terakado *et al.* (2017) further combined shutters, in addition to an active yaw system, to input a range of gusts in a full-scale automotive wind tunnel, whereas Wood *et al.* (2022) recently demonstrated a blockage-type device to alter a nozzle outlet for gust generation.

Active grids have increased in popularity for generating turbulence in experimental facilities. Active grids resembling those introduced by Makita (1991) tend to use a mesh of rods, which can be rotated and have attached elements or wings that obstruct the flow. Compared to traditional passive grids, as Mydlarski (2017) explained, most active grids can generate length scales exceeding the mesh length of the grid. Influential non-dimensional parameters affect turbulence produced by active grids and geometric parameters. One important non-dimensional parameter is the Rossby number, $\mathrm{Ro} = U/(\Omega M)$, where U is the mean velocity, Ω is the rotational rate of the grid elements, and M is the mesh length. Another significant non-dimensional parameter is the grid Reynolds number based on mesh length. Concerning geometry, the shape of the grid element, including its size and overall blockage, can affect the turbulent flow generated. Applications for active grid-generated turbulence are broad, and their capabilities to tailor flows are diverse. For example, the Makita-style active grid shown in Dogan *et al.* (2016) to create a turbulent freestream of various scales to study boundary layer behaviour was later used to generate bespoke shear profiles for experiments on model-scale wind turbines in a laboratory-scale wind tunnel (Hearst & Ganapathisubramani, 2017). Whereas Azzam & Lavoie (2023) used their active grid, formerly applied for turbulence studies (Hearst & Lavoie, 2015), for unsteady flow generation in a closed-loop, walled test-section wind tunnel.

The organization of this paper is as follows. The next section describes the novel TGS, its subsystems and the experimental methodologies. In the section that follows, selected results for each of the three TGS subsystems are presented and discussed. In particular, the results presented consider the resulting yaw distributions, gust response, and turbulence generation. The final section includes the concluding remarks.

SYSTEM AND METHODS

The Turbulence Generation System (TGS) described herein is a novel system comprising three subsystems housed within a single unit at the 400 mm x 625 mm nozzle opening of the 3/4 open-jet closed-loop one-tenth model wind tunnel at York University. The wind tunnel has a 6.8 to 1 contraction and a fan/motor capable of producing test section flow velocities up to approximately 70 m/s. The wind tunnel also has a heat exchanger to maintain flow temperatures inside the test section. The first subsystem of the TGS is an active grid responsible for generating broadband turbulence. The second subsystem is designed to produce unsteady streamwise flow, such as gusts. Finally, the third subsystem is designed to produce time-varying yaw. In the fully open state, the front view of the TGS can be seen in Figure 1(a). The solid grid elements used for the turbulence and gusting subsystems were placed on a mesh with approximately 25 mm spacing over the nozzle's height and 23 mm spacing in width. The active grid elements were nominally diamond shapes, 23.5 mm in diameter and 3.8 mm in width. The grid elements were manufactured using stereolithography printing. They were slid over 3.175 mm diameter steel rods aligned using a jig and glued in place. Similar in concept to that of the early design by Makita (1991) or as shown in Larssen & Devenport (2011), each of the rods was independently controlled. To create gusts in the freestream, the upper portion of the grid was decoupled from the lower along the verticle axis. Figure 1(b) shows the upper portion of vertical elements and five horizontal rows of grid elements closed. The active grid was designed to accommodate a 12-airfoil yaw subsystem between vertical active grid rods. A section view of the active flaps of the yaw subsystem is shown in Figure 1(c). Figure 1(d) shows a photograph of TGS components, such as the airfoils and grid elements. The resulting TGS is driven by 54 independent NEMA17 integrated step motors using custom-designed programs for operation.

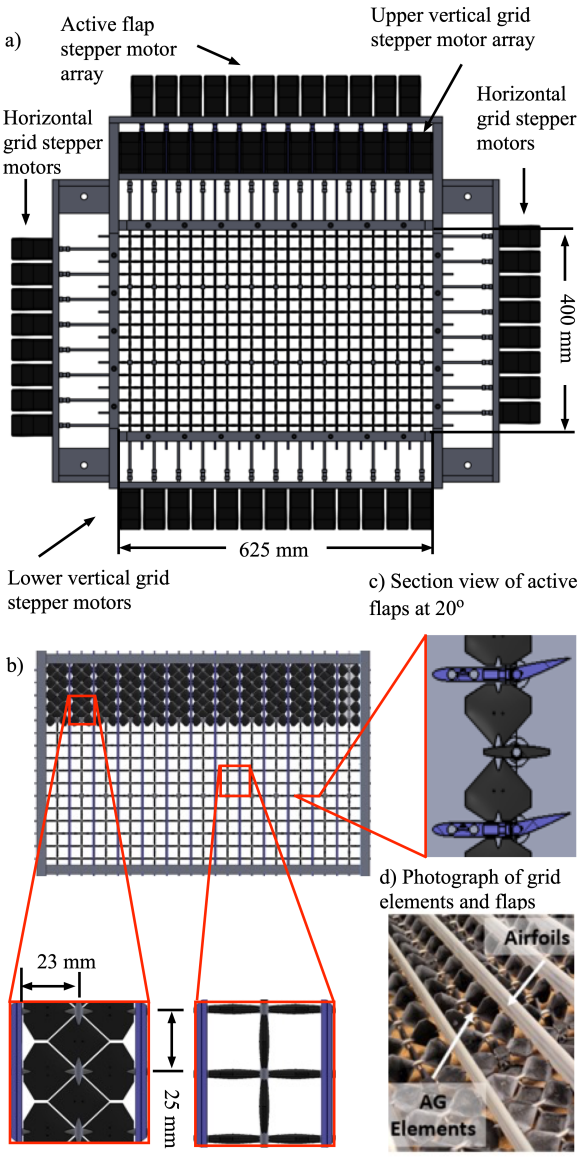

Figure 1. a) The front view of the TGS shows the motor, shaft locations and overall dimensions. b) The active gust system in the closed position for maximum gust generation. c) Section view showing an airfoil and flap and d) photograph of the grid elements and airfoils.

Flow measurements were acquired using two-component hot-wire anemometry. For the instantaneous streamwise and spanwise flow in the open wind tunnel testing section downstream of the TGS, a Dantec probe (55P11) operated by a Streamline Pro constant temperature anemometer was used. The hotwire was calibrated using the look-up table method (Burattini & Antonia, 2005), and the air temperature was continuously monitored throughout all experiments using a T-type Omega thermocouple in the freestream. The constant temperature anemometer and the reference pitot-static tube data were sampled at 20 kHz by a National Instruments cDAQ-9178 frame with two NI-9215 analog input modules. Low-pass filtering of all signals below the Nyquist frequency prevented the aliasing of each signal. Calibrations were performed immediately before and after each experiment. The uncertainties associated with the velocity measurements were calculated using standard analysis methodologies, including the accuracy of the reference velocity, goodness of the calibration fit and drift uncertainty. The uncertainty of the velocity measurements was within 2%. The airflow measurements were generally obtained at 10, 20, and 30 mesh lengths downstream of the grid. This covers the range in which a vehicle would be positioned relative to the nozzle in a comparable full-scale wind tunnel. The results presented were spatially averaged over 6 points in a repeating unit of the turbulence generation system geometry, approximately 5 mesh lengths from the floor of the 3/4 open-jet, or where would be the approximate mid-height of a vehicle in a full-scale wind tunnel.

RESULTS

The yaw subsystem underwent testing at various flap oscillation amplitudes ($\phi = \pm 5^\circ$ to 15°), to compare the flow response to forcing. The sample results were taken at an oscillation frequency of 1 Hz. Testing up to 15 Hz showed minor frequency effects in this range for the reference velocity of 15 m/s at the nozzle outlet. Figure 2(a) displays the phase-averaged response for these cases, whereas Figure 2(b) shows the resulting distribution of the flow angles.

As the flap amplitude increased, the flow angle also increased, but the responses began to deviate from the sinusoidal input waveform, which suggested a potential stall region. This was particularly noticeable in the larger oscillation amplitude cases. Tracking the vertical active grid elements with the flap angle improved the yaw oscillation performance; however, this result was not included in the figures since only the yaw subsystem was considered here.

The yaw distribution for the three amplitude cases is shown in Figure 2(b), in addition to the baseline case where the yaw subsystem was not activated. The flap amplitude and standard deviation of the measured distributions were strongly correlated, with standard deviations of approximately 2.1 degrees for the baseline and 3.0, 3.7, and 4.4 degrees observed with increasing flap amplitude values. On the other hand, a negative correlation was observed between the flap amplitude and the kurtosis of the distributions. With increasing flap amplitude values, Kurtosis decreased from approximately 2.9 for the baseline to 2.4 for the active case with the greatest amplitude. As previously noted, flow-turning performance was limited as the flap amplitude surpassed the stall region. As a result, instead of widening the distribution's tails, the range of instantaneous flow angles spread over the central region peak and, therefore, reduces the kurtosis.

The effect on yaw distribution was relatively minor over the tested range of yaw oscillation frequencies (not shown).

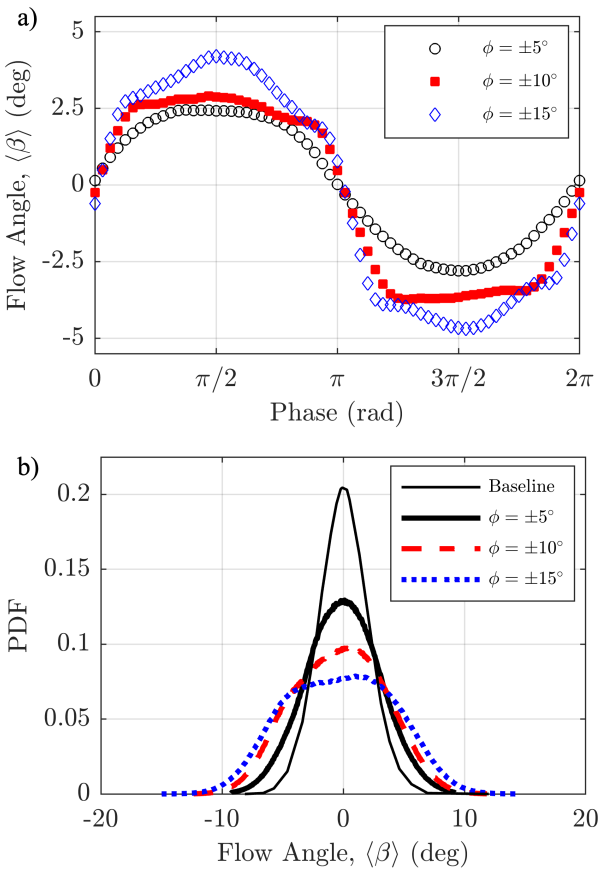

Figure 2. a) Phase-averaged response plots for yaw subsystem sinusoidal oscillation cases at different amplitudes and at 1 Hz. b) Corresponding flow angle distribution for active yaw oscillation cases with the additional static flap case.

Each measured distribution's standard deviation and kurtosis was approximately 3.8 and 2.5 respectively at $\phi = \pm 10^\circ$. As part of analyzing the effect of oscillation frequency, frequency scanning or modulation was also tested. This involved oscillating the flaps between $\phi = \pm 10^\circ$ with a dynamic frequency scaling between 0.5 to 12.5 Hz. The flow spectra based on the fluctuating streamwise and spanwise velocities are shown in Figure 3. All three fixed frequency cases have prominent peaks at their respective driving frequency and harmonics. Higher harmonics may be anticipated from the phase-averaged response cycle previously shown in Figure 2(a). Meanwhile, the frequency scanning mode demonstrates a new capability of the novel TGS, filling out the spectra over a range of frequencies within the scanning region. Thus, this operation mode can modify the resulting spectra without significantly affecting the yaw phase-averaged response and distribution.

The gusting subsystem was tested while the airfoils of the active yaw system were held in a static position with zero angle of attack. Various operating parameters, such as frequency and oscillation shapes, affected the performance of the gusting subsystem; however, for brevity, only the effect of the level of nozzle blockage is included herein. The gust subsystem comprises five horizontal shafts and thirteen partial-length vertical sets of elements. During testing, gusting elements were set to oscillate between positions parallel and perpendicular to the flow. For testing concerning the maximum level of blockage, the number of horizontal shafts making up the gusting system was reduced from the top five horizontal shafts (shown closed

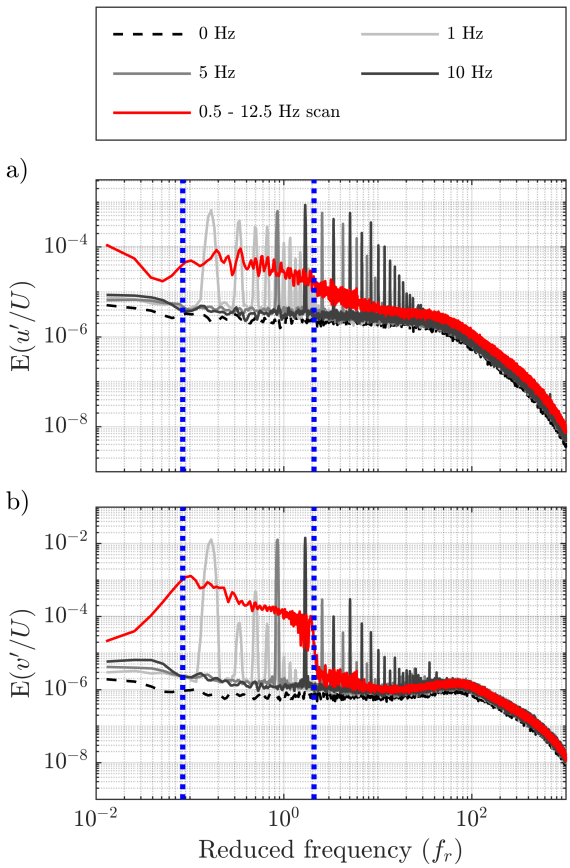

Figure 3. Streamwise a) and spanwise b) flow spectra. The spectra for the static case with flap angles at 0 degrees are given for reference. Results for the different discrete and scanning frequency cases are shown.

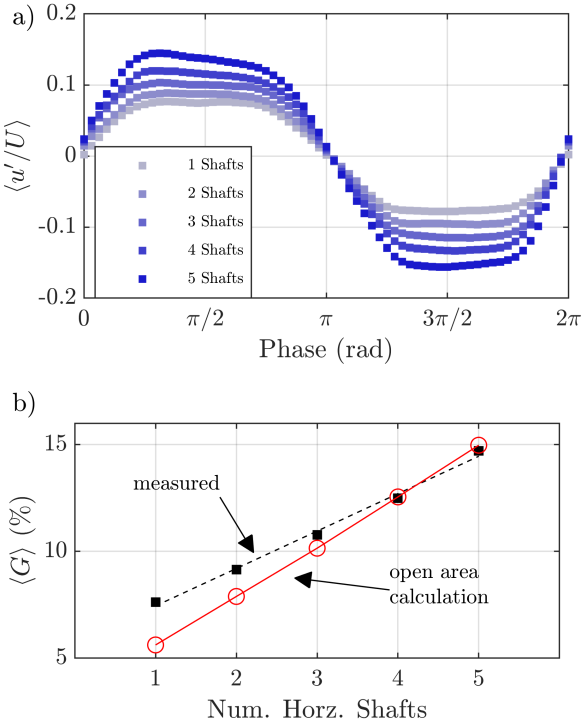

Figure 4. a) Phase-averaged flow velocity fluctuation cycles for different blockages. The number of shafts indicates how many horizontal shafts are actuated to block the flow. b) The gust percentage for different blockages.

in Figure 1b). The performance of the gust subsystem is discussed in terms of phase-averaged flow cycles and total gust amplitude relative to the mean.

The effect of varying the gust subsystem blockage was explored by varying the number of the active gust system horizontal shafts from one to five. All cases were tested with an oscillation frequency of 1 Hz, an amplitude between fully open and fully closed. The waveform applied to the gusting subsystem was a capped triangular type, having linear variations in position between open and closed, and held in the fully open or fully closed for a duration of $\pi/2$. The phase-averaged results shown in Figure 4(a) show increasing fluctuation amplitude with increasing blockage. Figure 4(b) shows a linear relationship between the gusting ratio, defined by the gust fluctuation amplitude normalized by the mean flow velocity, and the number of activated shafts. The gust percentage was higher than predicted based on the system's open area for the lower blockage levels, whereas it was slightly lower at the greatest blockage. While the open frontal area can not capture the effects of the losses associated with the flow through the gusting system or possible induced flow patterns within the nozzle, it provided a reasonable estimate of the gust percentage.

The upper and lower sections of the vertical rods were synchronized to test the active grid subsystem. The effect of changing the Rossby number on turbulence intensity, isotropy, length scale, and flow spectra is examined. For all results, the active grid subsystem was operated in a double random mode, a common approach to operate active grids, as explained, for example, in the review by Mydlarski (2017).

In Figure 5(a), the turbulence intensity is expressed as the intensity of the turbulent kinetic energy, as shown in comparison with results from Hearst & Lavoie (2015), where $q^2 = u'^2 + 2v'^2$. Hearst & Lavoie (2015) showed that for their system, the turbulence intensity increased sharply for Ro $<$ 30 before asymptotically plateauing for 50 $<$ Ro $<$ 150. The sharp increase seen in Hearst & Lavoie (2015) is not shown in the present results since measurements were not taken at these lower values of Ro. The relatively high turbulence values observed at 10M were consistent with Makita (1991), who measured values over 30% based on streamwise velocity fluctuations.

The anisotropic ratio in the streamwise and spanwise directions, $I = u'/v'$, is shown in Figure 5(b). With the grid fully open, the grid produces a flow with anisotropic ratios similar to that produced by a passive grid. The grid produced an anisotropic ratio of 1.4 and 1.23 at 10M and 20M, respectively, whereas Vita *et al.* (2018) reported anisotropic ratios of 1.14, 1.19, and 1.2 at 10M for three of their passive grids. The active grid produced anisotropic flow in the double random mode, reaching 2.23 at 10M. Generally, active grids with faster rotations show decreased anisotropy. The active grid used in this research consistently decreased the anisotropic ratio for each downstream plane. Performance trends suggest that lower Ro values can improve isotropy. As with other active grids, the TGS's active grid subsystem could affect the large scales (L_u) with Rossby numbers over a range where turbulence intensity changes tended to plateau. For example, as shown in Figure 5(c), with Ro $>$ 25, L_u/M increased by over a factor of 2.5, with Ro number increasing from approximately 25 to 110. A similar behaviour was indicated by Hearst & Lavoie (2015), where diamond grid elements and diamonds with holes are in-

cluded for comparison in the figure, and Larssen & Devenport (2011).

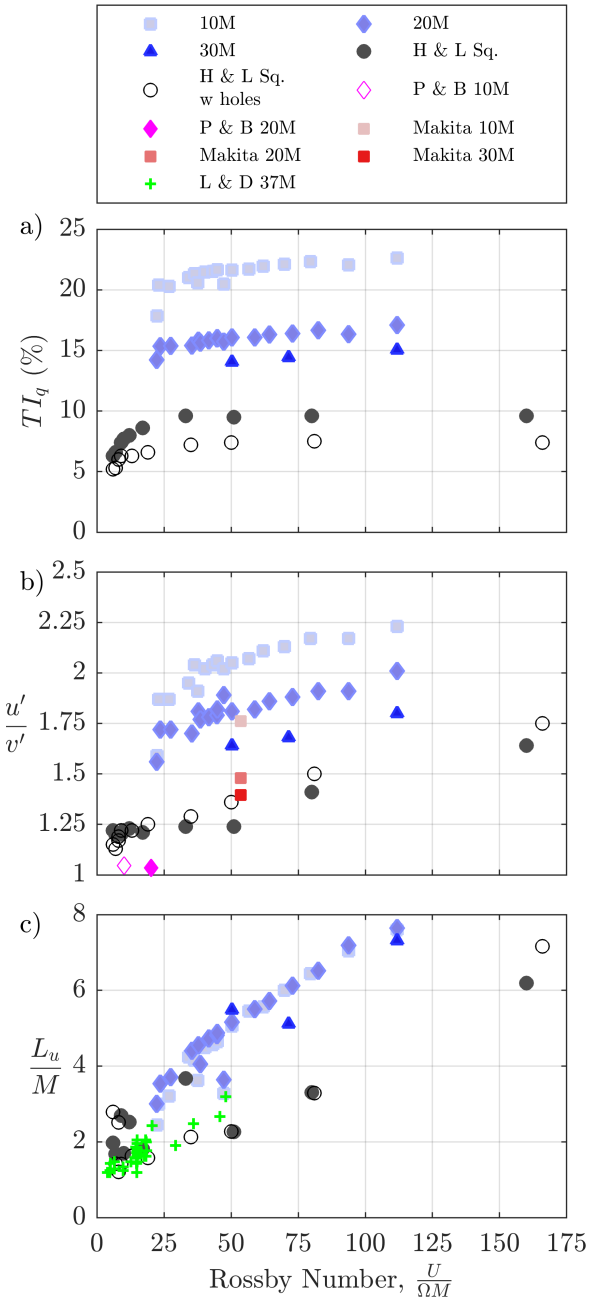

Figure 5. a) Variation of the turbulence intensity with Rossby number for cases at 10, 20 and 30 mesh lengths. Comparable data from Hearst & Lavoie (2015) at 30M with solid diamond grid elements and with holes are included for comparison. b) Corresponding measurements of the isotropy with comparisons from the literature, including results from Makita (1991) and Poorte & Biesheuvel (2002). c) Variation of the streamwise turbulence length scale with Rossby number, with data from Larssen & Devenport (2011).

A sufficiently high Taylor Reynolds number (Re_λ, where λ is the Taylor microscale or characteristic length scale used for this Reynolds number definition) is needed to achieve a broad spectrum of scales and to produce a well-defined inertial subrange (Mydlarski, 2017). Most laboratory wind tunnel facilities are limited to Taylor Reynolds numbers on the order of 10^3 due to size (Shen & Warhaft, 2000), and are often less. Nevertheless, the inertial subrange can still be viewed for $\mathrm{Re}_\lambda > 250$ Makita (1991). At 20M, the grid used in this research produced a maximum Taylor Reynolds number of $\mathrm{Re}_\lambda = 880$. The relatively high Taylor Reynolds numbers contributed to spectra with well-defined inertial subranges with slopes approaching the universal -5/3 slope. The lowest Taylor Reynolds number at 20M produced for the double random case measured $\mathrm{Re}_\lambda = 210$. The premultiplied spectra for three different cases and the grid held fully open in passive mode can be seen in Figure 6. The spectra have been premultiplied by the wave number ($\kappa = 2\pi f/U$) so that the total energy content is represented by the area under the curves. The test cases shown were from the double random mode, at 10M or 20M, with Ro values of 22, 45 and 111. For reference, with Ro = 45 at 20M, $\mathrm{Re}_\lambda > 732$, whereas for the grid fully open in passive mode, the produced Taylor Reynolds number was 70 at 20M for reference. The greater Reynolds numbers produced a wider inertial subrange.

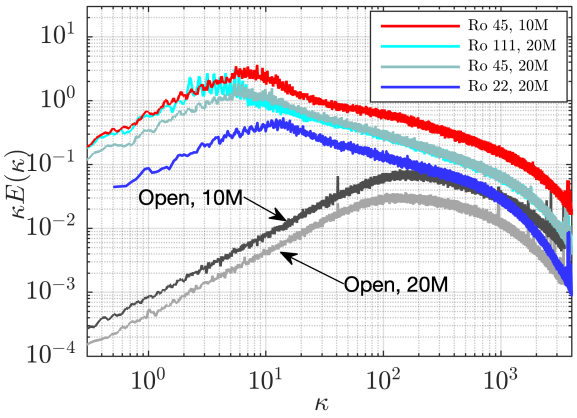

Figure 6. Premultiplied wavenumber spectra of the streamwise flow fluctuations for four active turbulence generation cases at Rossby numbers of 22, 45, and 111, and two static (passive) cases at 10M and 20M.

CONCLUDING REMARKS

The present experimental study demonstrates the capabilities of a novel turbulence generation system to produce a range of on-road flow conditions in a scale model 3/4 open jet, closed-loop wind tunnel. Three subsystems were designed to generate transient yaw, gusts, and turbulence to generate a range of flow conditions. The yaw subsystem was comprised of an array of airfoils with active flaps. The active grid subsystem was a Makita-style array of rotatable rods with grid elements; however, the active yaw subsystem displaced every other vertical bar of the grid. The active gust subsystem used five horizontal bars from the active grid, furthest from the floor of the test section, and the corresponding length of vertical bars. Each subsystem's effect on the resulting turbulent and unsteady flows was evaluated individually.

It was shown that the active yaw subsystem can generate a wide range of yaw distributions. The baseline open case resulted in a distribution with a standard deviation of 2.1 de-

grees, whereas this value increased up to 4 degrees with active forcing. Compared to discrete frequency forcing of the active yaw subsystem, frequency sweeping or modulation could fill out broad areas of the spectrum while having only a minimum influence on the yaw angle distribution. Initial testing of the active gust subsystem demonstrated streamwise velocity variations of up to 15 percent. The active turbulence system produced relatively strong turbulence levels. Rossby numbers greater than 20 were considered in the present study, and the turbulence length and length scales demonstrated increasing trends with this parameter.

The results shown in this study demonstrate the potential for such a system to generate complex and tailorable flow fields relevant to industrial problems, such as recreating on-road flow conditions in wind tunnels for vehicle aerodynamic testing. Future aspects of the research should include combining the effects of the subsystems on the resulting flow fields and modifications to target other moderate levels of turbulence.

REFERENCES

Azzam, A. & Lavoie, P. 2023 Unsteady flow generation in a wind tunnel using an active grid. *Experiments in Fluids* **64** (2), 29.

Blumrich, R., Widdecke, N., Wiedemann, J., Michelbach, A., Wittmeier, F. & Beland, O. 2015 New FKFS technology at the full-scale aeroacoustic wind tunnel of university of stuttgart. *SAE International Journal of Passenger Cars - Mechanical Systems* **8** (1).

Burattini, P. & Antonia, R. A. 2005 The effect of different x-wire calibration schemes on some turbulence statistics. *Experiments in fluids* **38**, 80–89.

Cogetti, A. 2003 Generation of a controlled level of turbulence in the Pininfarina wind tunnel for the measurement of unsteady aerodynamics and aeroacoustics. *SAE Transactions* **112**, 375–392.

Cooper, K. R. & Watkins, S. 2007 The unsteady wind environment of road vehicles, part one: A review of the on-road turbulent wind environment. In *SAE Technical Paper*.

Dogan, E., Hanson, R. E. & Ganapathisubramani, B. 2016 Interactions of large-scale free-stream turbulence with turbulent boundary layers. *Journal of Fluid Mechanics* **802**, 79–107.

Duncan, B., D'Alessio, L., Gargoloff, J. & Alajbegovic, A. 2017 Vehicle aerodynamics impact of on-road turbulence. *Proceedings of the Institution of Mechanical Engineers, Part D: Journal of Automobile Engineering* **231** (9), 1148–1159.

Hearst, R. J. & Ganapathisubramani, B. 2017 Tailoring incoming shear and turbulence profiles for lab-scale wind turbines. *Wind Energy* **20** (12), 2021–2035.

Hearst, R. J. & Lavoie, P. 2015 The effect of active grid initial conditions on high reynolds number turbulence. *Experiments in Fluids* **56** (10), 185.

Jessing, C., Wilhelmi, H., Wittmeier, F., Wagner, A., Wiedemann, J. & Dillmann, A. 2020 Investigation of transient aerodynamic effects on public roads in comparison to individual driving situations on a test site. *Tech. Rep.*. SAE Technical Paper 2020-01-0670.

Larssen, J. V. & Devenport, W. J. 2011 On the generation of large-scale homogeneous turbulence. *Experiments in Fluids* **50**, 1207–1223.

Makita, H. 1991 Realization of a large-scale turbulence field in a small wind tunnel. *Fluid Dynamics Research* **8** (1), 53–64.

McAuliffe, B. R., Belluz, L. & Belzile, M. 2014 Measurement of the on-road turbulence environment experienced by heavy duty vehicles. *SAE International Journal of Commercial Vehicles* **7** (2), 685–702.

Mydlarski, L. 2017 A turbulent quarter century of active grids: from Makita (1991) to the present. *Fluid Dynamics Research* **49** (6).

Poorte, R. E. G. & Biesheuvel, A. 2002 Experiments on the motion of gas bubbles in turbulence generated by an active grid. *Journal of Fluid Mechanics* **461**, 127–154.

Shen, X. & Warhaft, Z. 2000 The anisotropy of the small scale structure in high Reynolds number ($R_\lambda \sim 1000$) turbulent shear flow. *Physics of Fluids* **12** (11), 2976–2989.

Sims-Williams, D. B. 2011 Cross winds and transients: reality, simulation and effects. *SAE International Journal of Passenger Cars-Mechanical Systems* **4** (1), 172–183.

Terakado, S., Makihara, T., Sugiyama, T., Maeda, K., Tadakuma, K., Tsuboi, K., Iyota, M., Kosaka, K. & Sugiyama, S. 2017 Experimental investigation of aeroacoustic cabin noise in unsteady flow by means of a new turbulence generating device. *SAE International Journal of Passenger Cars-Mechanical Systems* **10** (2017-01-1545), 309–317.

Vita, G., Hemida, H., Andrianne, T. & Baniotopoulos, C. C. 2018 Generating atmospheric turbulence using passive grids in an expansion test section of a wind tunnel. *Journal of Wind Engineering and Industrial Aerodynamics* **178**, 91–104.

Wood, J. N., Breuer, M. & Neumann, T. 2022 A novel approach for artificially generating horizontal wind gusts based on a movable plate: The paddle. *Journal of Wind Engineering and Industrial Aerodynamics* **230**, 105170.

Wordley, S. & Saunders, J. 2009 On-road turbulence: Part 2. *SAE International Journal of Passenger Cars: Mechanical Systems* **2**, 111–137.